Computers in Biology and Medicine 45 (2014) 143–156

Contents lists available at ScienceDirect

Computers in Biology and Medicine

journal homepage: www.elsevier.com/locate/cbm

Numerical investigation of ultrasonic attenuation through 2D trabecular bone structures reconstructed from CT scans and random realizations

Robert P. Gilbert, Philippe Guyenne*, Jing Li

Department of Mathematical Sciences, University of Delaware, Newark, DE 19716, USA

ARTICLE INFO

Article history:
Received 11 September 2013
Accepted 10 December 2013

Keywords:
Cancellous bone
Random waves
Ultrasound
Viscoelastic material

ABSTRACT

In this paper, we compare ultrasound interrogations of actual CT-scanned images of trabecular bone with artificial randomly constructed bone. Even though it is known that actual bone does not have randomly distributed trabeculae, we find that the ultrasound attenuations are close enough to cast doubt on any microstructural information, such as trabeculae width and distance between trabeculae, being gleaned from such experiments. More precisely, we perform numerical simulations of ultrasound interrogation on cancellous bone to investigate the phenomenon of ultrasound attenuation as a function of excitation frequency and bone porosity. The theoretical model is based on acoustic propagation equations for a composite fluid-solid material and is solved by a staggered-grid finite-difference scheme in the time domain. Numerical experiments are performed on two-dimensional bone samples reconstructed from CT-scanned images of real human calcaneus and from random distributions of fluid-solid particles generated via the turning bands method. A detailed comparison is performed on various parameters such as the attenuation rate and speed of sound through the bone samples as well as the normalized broadband ultrasound attenuation coefficient. Comparing results from these two types of bone samples allows us to assess the role of bone microstructure in ultrasound attenuation. It is found that the random model provides suitable bone samples for ultrasound interrogation in the transverse direction of the trabecular network.

1. Introduction

Ultrasound has been considered as a means to characterize the elastic properties of cortical and cancellous bone for some time [1–32].

One experiment involves computing the spectrum of the phase velocity $c(f_c)$ and that of the attenuation rate $\alpha(f_c)$ where f_c is the frequency of the sound wave. Many investigations report that attenuation depends linearly on frequency from 200 kHz to 600 kHz and in the range of 600 kHz to 1 MHz [22,24,30,33]. Here we emulate some of these experiments in our computer simulations. In particular, we observe an approximately linear increase in attenuation over a wide range of frequencies, consistent with *in vitro* experiments of Wear [30].

Prior numerical work on this subject includes time-domain investigations by e.g. Hosakawa and Otani [17], Hosokawa [34], Buchanan et al. [35,36] and Bossy et al. [3,4,37]. In Hosokawa [34], three-dimensional simulations were performed with interrogations of cancellous bone in the main trabecular direction. Bossy et al. [37] also considered three-dimensional simulations with quasi-plane waves using a variant of the Graves method [38]. Frequency-domain investigations were conducted by e.g. Ilic et al. [39,40]. In this context, Klinge et al. [41] recently investigated ultrasound attenuation through cancellous bone, including the influence of wave reflection, using a homogenized finite-element model.

In the present paper, we examine ultrasound propagation through cancellous bone using the finite-difference time-domain approach described in [42,43]. More specifically, assuming that cancellous bone is a composite viscoelastic material with a prescribed distribution of fluid and solid points, we perform numerical simulations on two-dimensional bone samples obtained from CT-scanned images of human calcaneus and from realizations of a random process, to assess the phenomenon of ultrasound attenuation including its dependence on excitation frequency and bone volume fraction. For this purpose, a perfectly matched layer is introduced to minimize spurious wave reflection in the computational domain. The idea of using bone samples reconstructed from CT scans in numerical simulations was first proposed by Luo et al. [44].

* Corresponding author. Tel.: +1 3028318664.
E-mail addresses: gilbert@math.udel.edu (R.P. Gilbert), guyenne@math.udel.edu (P. Guyenne), jli@math.udel.edu (J. Li).

0010-4825/$ - see front matter © 2013 Elsevier Ltd. All rights reserved.
http://dx.doi.org/10.1016/j.compbiomed.2013.12.005

Currently, the problem of ultrasound propagation in cancellous bone is still not fully understood. In particular, the relationships between ultrasound parameters and bone properties are still not clearly established. Such information is needed in clinical examinations for better assessment of bone quality and for better diagnosis of such bone diseases as osteoporosis, using quantitative ultrasound techniques. With this in mind, the goal of the present study is two-fold:

- Assess the role of ultrasonic scattering by the trabecular network, following upon the work of Bossy et al. [37] who suggested that this mechanism is a major factor in ultrasonic attenuation. Indeed, cancellous bone is a heterogeneous medium with a very complex trabecular microstructure. Here we model this geometric feature by random realizations using the isotropic turning bands method [45], which allows for efficient numerical simulations with tunable parameters, and we carefully examine the relative effects of scattering versus viscosity.
- Test this random algorithm in view of generating a large catalog of viable, synthetic bone specimens (both *in vitro* and *in vivo*) to be used in a numerical procedure for solving the inverse problem of recovering effective bone parameters from acoustic interrogation. Despite recent progress [6,8,7], this inverse problem still represents a mathematical and computational challenge. This will be addressed in a future investigation. Here we test the random algorithm by comparing with results from CT scans of real bone on various ultrasonic quantities of clinical relevance, such as the attenuation rate and speed of sound (SOS) as well as the normalized broadband ultrasound attenuation (nBUA) coefficient.

Our numerical results support the claim that scattering by bone microstructure is a major component in ultrasound attenuation, even in two dimensions. Moreover, we observe that the measurements from CT scans and random realizations are similar, and consistent with existing results in the literature [30,37], which leads to expect that if instead of using isotropic random fields, we use orthotropic random fields, then the results may be even closer. This also casts doubt on the possibility of recovering any microstructural information, such as trabeculae width and distance between trabeculae, from acoustic interrogation of bone. Chaffai et al. [46] performed a correlation analysis on experimental data to evaluate the relationships between ultrasonic backscatter, density and microarchitecture of cancellous bone. They found no significant independent association between microstructure and backscatter coefficient (a microstructure-related ultrasonic parameter) after adjustment for density.

Recently, Meziere et al. [47] performed numerical simulations of ultrasound propagation through cancellous bone modeled by clusters of elliptic (two-dimensional) and ellipsoidal (three-dimensional) scatterers which are randomly distributed in an interstitial fluid. However, their random structures were synthesized by Monte Carlo generation, which is different from our turning bands method, and their study was not concerned with comparing results between real and synthetic bone. Bossy et al. [37] showed computations with bone samples reconstructed from CT scans of femural bone, but did not consider randomly generated samples. To our knowledge, a detailed comparison of numerical results based on CT scans and randomly generated structures of bone is reported for the first time here.

The paper is organized as follows: a viscoelastic model for ultrasound propagation through cancellous bone is presented in Section 2, and this model is reformulated in terms of the stress and velocity variables in Section 3. For the absorbing boundary conditions, we introduce perfectly matched layers in Section 4. Section 5 recalls the staggered-grid finite-difference scheme to discretize the resulting equations and Section 6 describes the two types of bone samples used in our investigation. Finally, we perform and discuss a number of numerical simulations on ultrasound attenuation using these bone samples in Section 7.

2. Viscoelastic model

Cancellous bone may be thought of as consisting of a solid matrix (trabeculae) filled with an interstitial fluid (blood marrow *in vivo* or water *in vitro*). In the present model, we assume a representative volume element of cancellous bone is the union of fluid and solid regions where the fluid region (denoted by the superscript f) obeys Stokes flow while the solid region (denoted by the superscript s) is a viscoelastic material. We only consider linear viscoelasticity without memory.

More precisely, the constitutive equations for the solid part (i.e. the trabeculae) are given by

$$\boldsymbol{\tau}^{(s)} = A^{(s)}\boldsymbol{e}(\mathbf{u}) + B^{(s)}\boldsymbol{e}(\mathbf{v}),$$

for the stress tensor, where

$$e(\mathbf{u})_{ij} = \frac{1}{2}\left(\frac{\partial u_i}{\partial x_j} + \frac{\partial u_j}{\partial x_i}\right), \quad e(\mathbf{v})_{ij} = \frac{1}{2}\left(\frac{\partial v_i}{\partial x_j} + \frac{\partial v_j}{\partial x_i}\right), \tag{2.1}$$

and $\mathbf{u}$ and $\mathbf{v}$ are the displacement and velocity fields, respectively.

These constitutive equations may be written in the generalized form:

$$\tau_{ij}^{(s)} = A_{ijkl}^{(s)} e(\mathbf{u})_{kl} + B_{ijkl}^{(s)} e(\mathbf{v})_{kl}, \tag{2.2}$$

where the $A_{ijkl}^{(s)}$ are elasticity coefficients with the classical symmetry and positivity properties:

$$A_{ijkl}^{(s)} e_{ij} e_{kl} \geq 0 \quad \text{and} \quad A_{ijkl}^{(s)} = A_{klij}^{(s)} = A_{jikl}^{(s)} = A_{ijlk}^{(s)},$$

while the $B_{ijkl}^{(s)}$ correspond to instantaneous viscosity terms with similar properties. In the isotropic elastic plane-strain case, we have

$$A_{ijkl}^{(s)} e_{kl} = (\lambda^{(1)}\delta_{ij}\delta_{kl} + 2\mu^{(1)}\delta_{ik}\delta_{jl}) e_{kl} = \lambda^{(1)}\delta_{ij} e_{kk} + 2\mu^{(1)} e_{ij},$$

where $\{\lambda^{(1)}, \mu^{(1)}\}$ are the Lamé parameters, and

$$B_{ijkl}^{(s)} e_{kl} = (\lambda^{(2)}\delta_{ij}\delta_{kl} + 2\mu^{(2)}\delta_{ik}\delta_{jl}) e_{kl} = \lambda^{(2)}\delta_{ij} e_{kk} + 2\mu^{(2)} e_{ij}, \tag{2.3}$$

where $\{\lambda^{(2)}, \mu^{(2)}\}$ are viscosity parameters, or more compactly

$$\boldsymbol{\tau}^{(s)} = \lambda^{(1)}\mathbb{I} e(\mathbf{u}) + 2\mu^{(1)}\boldsymbol{e}(\mathbf{u}) + \lambda^{(2)}\mathbb{I} e(\mathbf{v}) + 2\mu^{(2)}\boldsymbol{e}(\mathbf{v}), \tag{2.4}$$

with e being the dilatation, $\boldsymbol{e}$ the strain tensor and $\mathbb{I}$ the identity tensor. The equations of motion for the solid part are given by

$$\partial_t \mathbf{v} = b^{(s)}\ \mathrm{div}[A^{(s)}\boldsymbol{e}(\mathbf{u}) + B^{(s)}\boldsymbol{e}(\mathbf{v})], \tag{2.5}$$

in $\Omega_s \times [0, T]$, where $b^{(s)} = 1/\rho^{(s)}$ and $\rho^{(s)}$ are the solid buoyancy and density respectively. In the case where the material is isotropic, these equations take the form:

$$\partial_t \mathbf{v} = b^{(s)}\left[\frac{\partial}{\partial x_j}(\lambda^{(1)}\delta_{ij} e_{kk}(\mathbf{u}) + 2\mu^{(1)} e_{ij}(\mathbf{u})) + \frac{\partial}{\partial x_j}(\lambda^{(2)}\delta_{ij} e_{kk}(\mathbf{v}) + 2\mu^{(2)} e_{ij}(\mathbf{v}))\right]. \tag{2.6}$$

In the fluid part, by using the small compressibility approximation, the constitutive equations also take the form (2.2), namely

$$\boldsymbol{\tau}^{(f)} = A^{(f)}\boldsymbol{e}(\mathbf{u}) + B^{(f)}\boldsymbol{e}(\mathbf{v}),$$

with

$$A^{(f)} = c^2\rho^{(f)}\mathbb{I}, \quad B^{(f)} = 2\eta\mathbb{I},$$

where c is the speed of sound in the fluid and η is the fluid dynamic viscosity. The equations of motion for this Stokes system

read

$$\partial_t \mathbf{v} = b^{(f)}\ \mathrm{div}\left[c^2\rho^{(f)}\mathrm{div}(\mathbf{u})\mathbb{I} + 2\eta \boldsymbol{e}(\mathbf{v})\right], \tag{2.7}$$

in $\Omega_f \times [0,T]$, where $b^{(f)} = 1/\rho^{(f)}$ and $\rho^{(f)}$ are the fluid buoyancy and density respectively.

In both fluid and solid parts, the system of equations for $\boldsymbol{\tau}$, $\mathbf{v}$ and $\mathbf{u}$ is completed by

$$\partial_t \mathbf{u} = \mathbf{v}. \tag{2.8}$$

Free-surface conditions are imposed at the boundary of the full domain $\Omega_f \cup \Omega_s$. Continuity of displacements, velocities and forces is assumed at the fluid–solid interface. This is completed by initial conditions $\boldsymbol{\tau} = \boldsymbol{\tau}_0$, $\mathbf{v} = \mathbf{v}_0$ and $\mathbf{u} = \mathbf{u}_0$ at $t = 0$. For ultrasound excitations by a pressure source as in Section 7.2, we set $\boldsymbol{\tau}_0 = \mathbf{0}$, $\mathbf{v}_0 = \mathbf{0}$ and $\mathbf{u}_0 = \mathbf{0}$.

These are the linearized equations for acoustic propagation through a composite fluid-solid material, which are solved in our numerical simulations.

3. Stress–velocity formulation

Since the trabeculae is assumed to be viscoelastic and isotropic, this leads to a system of equations similar to that in Graves [38] for seismic waves. Considering the two-dimensional case in Cartesian coordinates (x,y), the stresses in the trabeculae may be written as

$$\begin{aligned}
\tau_{xx}^{(s)} &= (\lambda^{(1)} + 2\mu^{(1)})\partial_x u_x + \lambda^{(1)}\partial_y u_y \\
&\quad + (\lambda^{(2)} + 2\mu^{(2)})\partial_x v_x + \lambda^{(2)}\partial_y v_y, \\
\tau_{yy}^{(s)} &= (\lambda^{(1)} + 2\mu^{(1)})\partial_y u_y + \lambda^{(1)}\partial_x u_x \\
&\quad + (\lambda^{(2)} + 2\mu^{(2)})\partial_y v_y + \lambda^{(2)}\partial_x v_x, \\
\tau_{xy}^{(s)} &= \mu^{(1)}(\partial_x u_y + \partial_y u_x) + \mu^{(2)}(\partial_x v_y + \partial_y v_x),
\end{aligned} \tag{3.1}$$

and their evolution obeys

$$\begin{aligned}
\partial_t \tau_{xx}^{(s)} &= (\lambda^{(1)} + 2\mu^{(1)})\partial_x v_x + \lambda^{(1)}\partial_y v_y \\
&\quad + (\lambda^{(2)} + 2\mu^{(2)})\partial_x \dot{v}_x + \lambda^{(2)}\partial_y \dot{v}_y, \\
\partial_t \tau_{yy}^{(s)} &= (\lambda^{(1)} + 2\mu^{(1)})\partial_y v_y + \lambda^{(1)}\partial_x v_x \\
&\quad + (\lambda^{(2)} + 2\mu^{(2)})\partial_y \dot{v}_y + \lambda^{(2)}\partial_x \dot{v}_x, \\
\partial_t \tau_{xy}^{(s)} &= \mu^{(1)}(\partial_x v_y + \partial_y v_x) + \mu^{(2)}(\partial_x \dot{v}_y + \partial_y \dot{v}_x),
\end{aligned} \tag{3.2}$$

where ∂_t denotes the partial derivative with respect to time t, and (∂_x, ∂_y) denote the partial derivatives with respect to the spatial coordinates (x,y) respectively. Moreover, to avoid overly clumsy expressions, the upper dot is further shorthand notation for ∂_t (e.g. $\dot{v}_x = \partial_t v_x$). In (3.2), the acceleration field is given by

$$\begin{aligned}
\partial_t v_x &= b^{(s)}[\partial_x \tau_{xx}^{(s)} + \partial_y \tau_{xy}^{(s)}], \\
\partial_t v_y &= b^{(s)}[\partial_x \tau_{xy}^{(s)} + \partial_y \tau_{yy}^{(s)}].
\end{aligned} \tag{3.3}$$

In the interstitial fluid, the evolution equations for the stress field are

$$\begin{aligned}
\partial_t \tau_{xx}^{(f)} &= c^2\rho^{(f)}(\partial_x v_x + \partial_y v_y) + 2\eta\partial_x \dot{v}_x, \\
\partial_t \tau_{yy}^{(f)} &= c^2\rho^{(f)}(\partial_x v_x + \partial_y v_y) + 2\eta\partial_y \dot{v}_y, \\
\partial_t \tau_{xy}^{(f)} &= \eta(\partial_x \dot{v}_y + \partial_y \dot{v}_x),
\end{aligned} \tag{3.4}$$

combined with

$$\begin{aligned}
\partial_t v_x &= b^{(f)}[\partial_x \tau_{xx}^{(f)} + \partial_y \tau_{xy}^{(f)}], \\
\partial_t v_y &= b^{(f)}[\partial_x \tau_{xy}^{(f)} + \partial_y \tau_{yy}^{(f)}].
\end{aligned} \tag{3.5}$$

We note that both the fluid and solid phases are described by a general system of the form:

$$\begin{aligned}
\tau_{xx}^{(a)} &= (\lambda^{(k)} + 2\mu^{(k)})\partial_x u_x + \lambda^{(k)}\partial_y u_y \\
&\quad + (\lambda^{(k+1)} + 2\mu^{(k+1)})\partial_x v_x + \lambda^{(k+1)}\partial_y v_y, \\
\tau_{yy}^{(a)} &= (\lambda^{(k)} + 2\mu^{(k)})\partial_y u_y + \lambda^{(k)}\partial_x u_x \\
&\quad + (\lambda^{(k+1)} + 2\mu^{(k+1)})\partial_y v_y + \lambda^{(k+1)}\partial_x v_x, \\
\tau_{xy}^{(a)} &= \mu^{(k)}(\partial_x u_y + \partial_y u_x) + \mu^{(k+1)}(\partial_x v_y + \partial_y v_x),
\end{aligned} \tag{3.6}$$

together with the evolution equations

$$\begin{aligned}
\partial_t \tau_{xx}^{(a)} &= (\lambda^{(k)} + 2\mu^{(k)})\partial_x v_x + \lambda^{(k)}\partial_y v_y \\
&\quad + (\lambda^{(k+1)} + 2\mu^{(k+1)})\partial_x \dot{v}_x + \lambda^{(k+1)}\partial_y \dot{v}_y, \\
\partial_t \tau_{yy}^{(a)} &= (\lambda^{(k)} + 2\mu^{(k)})\partial_y v_y + \lambda^{(k)}\partial_x v_x \\
&\quad + (\lambda^{(k+1)} + 2\mu^{(k+1)})\partial_y \dot{v}_y + \lambda^{(k+1)}\partial_x \dot{v}_x, \\
\partial_t \tau_{xy}^{(a)} &= \mu^{(k)}(\partial_x v_y + \partial_y v_x) + \mu^{(k+1)}(\partial_x \dot{v}_y + \partial_y \dot{v}_x),
\end{aligned} \tag{3.7}$$

where $(a,k) = \{(s,1),(f,3)\}$, $\lambda^{(3)} = c^2\rho^{(f)}$, $\lambda^{(4)} = 0$, $\mu^{(3)} = 0$ and $\mu^{(4)} = \eta$. The symbol (a) refers to either fluid or solid depending on which phase is considered. From a numerical point of view as described below, each grid point is thus either fluid or solid, and satisfies the corresponding equations.

The acceleration field also has the same form for both phases:

$$\begin{aligned}
\partial_t v_x &= b^{(a)}[\partial_x \tau_{xx}^{(a)} + \partial_y \tau_{xy}^{(a)}], \\
\partial_t v_y &= b^{(a)}[\partial_x \tau_{xy}^{(a)} + \partial_y \tau_{yy}^{(a)}],
\end{aligned} \tag{3.8}$$

and this is completed by

$$\partial_t u_x = v_x, \quad \partial_t u_y = v_y, \tag{3.9}$$

which yields the displacements in both phases as well.

4. Perfectly matched layer

In all of our applications, the domain (i.e. the bone sample) is assumed to be rectangular. To simulate ultrasound propagation, a signal is emitted by a source from one side of the domain and recorded by a receiver on the opposite side. Free-surface boundary conditions are specified as in [42], except on the receiver side where an absorbing boundary condition is imposed. The reason for this is to prevent spurious wave reflection which may contaminate the calculation of ultrasound attenuation rate as described below [37]. For this purpose, we adopt the approach of perfectly matched layers (PMLs) which has proved to be effective in finite-difference and finite-element methods for simulation of linear electromagnetic and acoustic waves in the time domain [48]. In particular, Collino and Tsogka [49] adapted this approach to the stress–velocity formulation of elastodynamics. Here we apply their method to our bone problem and adapt it to our staggered-grid finite-difference scheme. A perfectly matched layer is an artificial region adjacent to the actual domain and is designed in such a way that no reflection is produced at the interface between the two media. In practice, a relatively thin layer with strong damping parameters may be used to save computational cost.

Following [49], we decompose the stress and velocity components as

$$\tau_{ij}^{(a)} = \tau_{ij}^{(a)\perp} + \tau_{ij}^{(a)\parallel}, \quad v_j = v_j^{\perp} + v_j^{\parallel},$$

so that their evolution equations read as follows:

$$\partial_t \tau_{xx}^{(a)\perp} + d(x)\tau_{xx}^{(a)\perp} = (\lambda^{(k)} + 2\mu^{(k)})\partial_x v_x + (\lambda^{(k+1)} + 2\mu^{(k+1)})\partial_x \dot{v}_x,$$

$$\partial_t \tau_{yy}^{(a)\perp} + d(x)\tau_{yy}^{(a)\perp} = \lambda^{(k)}\partial_x v_x + \lambda^{(k+1)}\partial_x \dot{v}_x,$$
$$\partial_t \tau_{xy}^{(a)\perp} + d(x)\tau_{xy}^{(a)\perp} = \mu^{(k)}\partial_x v_y + \mu^{(k+1)}\partial_x \dot{v}_y,$$
$$\partial_t v_x^{\perp} + d(x)v_x^{\perp} = b^{(a)}\partial_x \tau_{xx}^{(a)},$$
$$\partial_t v_y^{\perp} + d(x)v_y^{\perp} = b^{(a)}\partial_x \tau_{xy}^{(a)}, \tag{4.1}$$

for the derivatives perpendicular to the interface with the PML, and

$$\partial_t \tau_{xx}^{(a)\parallel} = \lambda^{(k)}\partial_y v_y + \lambda^{(k+1)}\partial_y \dot{v}_y,$$
$$\partial_t \tau_{yy}^{(a)\parallel} = (\lambda^{(k)} + 2\mu^{(k)})\partial_y v_y + (\lambda^{(k+1)} + 2\mu^{(k+1)})\partial_y \dot{v}_y,$$
$$\partial_t \tau_{xy}^{(a)\parallel} = \mu^{(k)}\partial_y v_x + \mu^{(k+1)}\partial_y \dot{v}_x,$$
$$\partial_t v_x^{\parallel} = b^{(a)}\partial_y \tau_{xy}^{(a)},$$
$$\partial_t v_y^{\parallel} = b^{(a)}\partial_y \tau_{yy}^{(a)}, \tag{4.2}$$

for the derivatives parallel to this interface. In writing (4.1) and (4.2), we assume waves propagate mainly in the x-direction and thus the PML is adjacent to a y-side of the domain. Therefore, the symbol $\perp$ refers to the x-direction while the symbol $\parallel$ refers to the y-direction. The damping function $d(x)$ is taken to be zero everywhere except in the PML, hence system (4.1) and (4.2) is equivalent to (3.7) and (3.8) in the interior region, by linearity. A similar procedure can be followed for absorption in the y-direction.

5. Discretized equations

Following [38,42,43], we use a staggered-grid finite-difference scheme to discretize system (4.1) and (4.2) in each phase, where the various components of displacement, velocity and stress are defined at different grid points in the computational domain. A sketch of a unit cell constituting the building block of the computational domain shows the grid layout in Fig. 1. This method is staggered and second-order in both space and time. In the following expressions, subscripts refer to the spatial indices while superscripts refer to the time index. For example,

$$v_{xi+1/2,j}^{n+1/2}$$

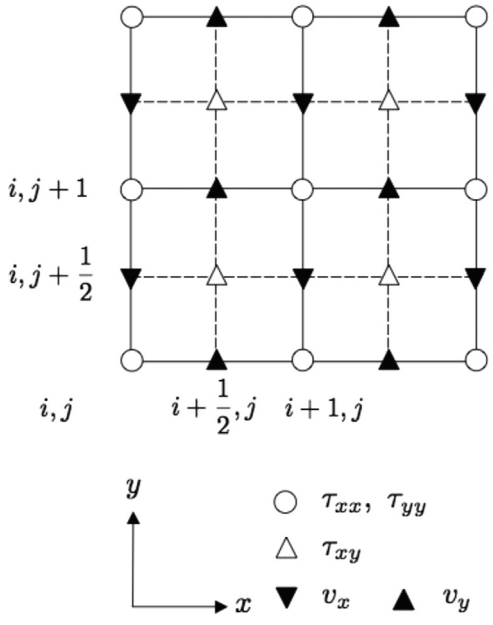

Fig. 1. Sketch of four unit cells in the two-dimensional staggered grid. The different nodes for the various physical variables are also labeled in each cell. Note that the displacement and velocity components are evaluated at the same respective nodes.

represents the x-component of the velocity at point $x_{i+1/2} = (i+1/2)\Delta x$, $y_j = j\Delta y$ and at time $t_{n+1/2} = (n+1/2)\Delta t$, where Δx, Δy are the mesh sizes in the two spatial directions and Δt is the time step. To avoid overly cumbersome expressions, D_j denotes the difference operator for the discretization of the partial derivative ∂_j in space. Below we briefly present the discretized equations in the present context with a PML and refer the reader to [38,42] for further details on these difference operators. In particular, convergence tests of this numerical scheme for a related acoustic model of cancellous bone were performed in [42,43] (without PML). Because we assume continuity of displacements, velocities and forces across phases, the difference formulas may involve values at neighboring points located in different phases.

The discretization of (4.1) leads to

$$\frac{(\tau_{xx}^{(a)\perp})_{i,j}^{n+1} - (\tau_{xx}^{(a)\perp})_{i,j}^{n}}{\Delta t} + d(x_i)\frac{(\tau_{xx}^{(a)\perp})_{i,j}^{n+1} + (\tau_{xx}^{(a)\perp})_{i,j}^{n}}{2} = [(\lambda^{(k)} + 2\mu^{(k)})D_x v_x + (\lambda^{(k+1)} + 2\mu^{(k+1)})D_x \dot{v}_x]_{i,j}^{n+1/2},$$
$$\frac{(\tau_{yy}^{(a)\perp})_{i,j}^{n+1} - (\tau_{yy}^{(a)\perp})_{i,j}^{n}}{\Delta t} + d(x_i)\frac{(\tau_{yy}^{(a)\perp})_{i,j}^{n+1} + (\tau_{yy}^{(a)\perp})_{i,j}^{n}}{2} = [\lambda^{(k)}D_x v_x + \lambda^{(k+1)}D_x \dot{v}_x]_{i,j}^{n+1/2},$$
$$\frac{(\tau_{xy}^{(a)\perp})_{i+1/2,j+1/2}^{n+1} - (\tau_{xy}^{(a)\perp})_{i+1/2,j+1/2}^{n}}{\Delta t} + d(x_{i+1/2})\frac{(\tau_{xy}^{(a)\perp})_{i+1/2,j+1/2}^{n+1} + (\tau_{xy}^{(a)\perp})_{i+1/2,j+1/2}^{n}}{2} = [\mu^{(k)}D_x v_y + \mu^{(k+1)}D_x \dot{v}_y]_{i+1/2,j+1/2}^{n+1/2},$$
$$\frac{(v_x^{\perp})_{i+1/2,j}^{n+1/2} - (v_x^{\perp})_{i+1/2,j}^{n-1/2}}{\Delta t} + d(x_{i+1/2})\frac{(v_x^{\perp})_{i+1/2,j}^{n+1/2} + (v_x^{\perp})_{i+1/2,j}^{n-1/2}}{2} = [b^{(a)}D_x \tau_{xx}^{(a)}]_{i+1/2,j}^{n},$$
$$\frac{(v_y^{\perp})_{i,j+1/2}^{n+1/2} - (v_y^{\perp})_{i,j+1/2}^{n-1/2}}{\Delta t} + d(x_i)\frac{(v_y^{\perp})_{i,j+1/2}^{n+1/2} + (v_y^{\perp})_{i,j+1/2}^{n-1/2}}{2} = [b^{(a)}D_x \tau_{xy}^{(a)}]_{i,j+1/2}^{n}, \tag{5.1}$$

and that of (4.2) yields

$$\frac{(\tau_{xx}^{(a)\parallel})_{i,j}^{n+1} - (\tau_{xx}^{(a)\parallel})_{i,j}^{n}}{\Delta t} = [\lambda^{(k)}D_y v_y + \lambda^{(k+1)}D_y \dot{v}_y]_{i,j}^{n+1/2},$$
$$\frac{(\tau_{yy}^{(a)\parallel})_{i,j}^{n+1} - (\tau_{yy}^{(a)\parallel})_{i,j}^{n}}{\Delta t} = [(\lambda^{(k)} + 2\mu^{(k)})D_y v_y + (\lambda^{(k+1)} + 2\mu^{(k+1)})D_y \dot{v}_y]_{i,j}^{n+1/2},$$
$$\frac{(\tau_{xy}^{(a)\parallel})_{i+1/2,j+1/2}^{n+1} - (\tau_{xy}^{(a)\parallel})_{i+1/2,j+1/2}^{n}}{\Delta t} = [\mu^{(k)}D_y v_x + \mu^{(k+1)}D_y \dot{v}_x]_{i+1/2,j+1/2}^{n+1/2},$$
$$\frac{(v_x^{\parallel})_{i+1/2,j}^{n+1/2} - (v_x^{\parallel})_{i+1/2,j}^{n-1/2}}{\Delta t} = [b^{(a)}D_y \tau_{xy}^{(a)}]_{i+1/2,j}^{n},$$
$$\frac{(v_y^{\parallel})_{i,j+1/2}^{n+1/2} - (v_y^{\parallel})_{i,j+1/2}^{n-1/2}}{\Delta t} = [b^{(a)}D_y \tau_{yy}^{(a)}]_{i,j+1/2}^{n}. \tag{5.2}$$

As proposed by [49], we use a damping function of the form:

$$d(x) = d_0\left(\frac{x}{\delta}\right)^2,$$

with

$$d_0 = \frac{3V}{2\delta}\log\left(\frac{1}{R}\right),$$

where R is the theoretical reflection coefficient, δ is the PML width and V is a representative velocity. In this case, Collino and Tsogka [49] found that the simulated reflection coefficient is about 1%, 0.1% and 0.01% for $\delta = 5\Delta x$, $10\Delta x$ and $20\Delta x$ respectively.

Eqs. (5.1) and (5.2) form a closed system of equations for the stress and velocity fields. An auxiliary computation determines the displacements from the velocities at every time step, assuming that their respective components are defined at the same grid points but staggered temporally. Using centered finite differences in time, the discretization of (3.9) is

$$u^{n+1}_{xi+1/2,j} = u^{n}_{xi+1/2,j} + \Delta t v^{n+1/2}_{xi+1/2,j},$$
$$u^{n+1}_{yi,j+1/2} = u^{n}_{yi,j+1/2} + \Delta t v^{n+1/2}_{yi,j+1/2}. \tag{5.3}$$

6. Simulated bone samples

In the present model, the domain is a given distribution of points which are either fluid or solid. Numerically, this distribution of grid points is specified in two different ways: as a random distribution according to the turning bands method of Mantoglou and Wilson [45,50] and from digitized CT-scanned images of real human calcaneus. An example of such CT-scanned images, in a transverse plane of the foot, is shown in Fig. 5 with the top, bottom, right and left sides of the image corresponding to the anterior, posterior, lateral and medial aspects of the calcaneal bone respectively. A rectangular cross-section along this bone specimen is typically used in our numerical simulations. For this purpose, the original grayscale image is segmented to yield a binary mapping of the trabecular architecture (black for fluid and white for solid), as depicted in Fig. 5. Bone porosity is estimated from these binary images by evaluating the proportion of black pixels relative to the total number of pixels. In view of applications to quantitative ultrasound techniques for diagnosis of such bone diseases as osteoporosis, we focus our attention on bone samples of relatively high porosity.

Synthetic bone samples are simulated by using the turning bands method [45,50] which generates multidimensional stationary random fields with a prescribed covariance structure. This numerical approach is particularly efficient because, instead of generating a multidimensional field directly, several independent one-dimensional processes are simulated and superimposed. Below we briefly recall how we adapt this approach to our bone problem and refer the reader to [43,45] for further details. An example of two-dimensional random field so-obtained is presented in Fig. 6, where each point is normally distributed and the two-dimensional statistics obey an exponential covariance structure. To turn the random field into a distribution of fluid and solid points, we need to come up with a procedure to select which values of this field correspond to fluid or solid points for a prescribed porosity β. Since the field value at each point is normally distributed, this categorization can be achieved by using the error function:

$$\mathrm{erf}(z) = \frac{2}{\sqrt{\pi}} \int_0^z e^{-t^2}\, dt,$$

which is related to the cumulative density function of a standard normal distribution by

$$\Phi(z) = \frac{1}{2} + \frac{1}{2}\,\mathrm{erf}\left(\frac{z}{\sqrt{2}}\right). \tag{6.1}$$

Suppose z_0 is the critical point such that the probability:

$$\mathbb{P}(-z_0 < z < z_0) = \Phi(z_0) - \Phi(-z_0) = \beta,$$

then z_0 can be found by using (6.1) as

$$z_0 = \sqrt{2}\,\mathrm{erf}^{-1}(\beta).$$

Therefore a point in the domain is fluid if its field value is in $[-z_0, z_0]$, otherwise it is a solid point. By this selection, we can guarantee that a proportion of β points out of the total number is fluid. If the normal probability distribution is not standard, then we can always make it so by a change of variables.

Based on the two-dimensional realization of Fig. 6, we show examples of random distributions of fluid–solid points for $\beta = 0.7$, 0.75, 0.8 and 0.85 in Fig. 7(e)–(h), using the categorization described above. As expected, the proportion of fluid points increases with β similar to real bone samples. The main difference between these two types of bone samples is that the real ones exhibit a more anisotropic trabecular structure at lower porosity, with a preferred orientation in the vertical direction according to the CT-scanned images. Indeed, real cancellous bone is known to be an anisotropic heterogeneous material made of a complex network of interconnected plates and rods, while the simulated random one looks like an isotropic collection of solid patches among a fluid background. The synthetic bone samples however tend to look more and more like real ones as the porosity increases, which is consistent with the disappearance of the trabecular matrix during the osteoporosis process.

In the next section, comparing numerical results from these two types of bone samples allows us to assess the role of bone microstructure in ultrasound attenuation through the process of scattering. This is also a way to test the use of homogenization in effective acoustic models of cancellous bone [51–53] and thus whether information on bone properties (including the microstructure) can be effectively inferred from such models.

7. Numerical tests

Because of the large disparity in orders of magnitude between the various physical parameters in the problem, we find it convenient to non-dimensionalize the equations by using the characteristic length scale $\mathcal{L} = 10^{-2}$ m related to the size of the bone specimen and the characteristic time scale $\mathcal{T} = 10^{-5}$ s in the ultrasonic range. Therefore, unless stated otherwise, it is understood that values of dimensional quantities specified without physical units are dimensionless values relative to these characteristic scales.

Typical values of the physical parameters in the model are listed in Tables 1 and 2. The Lamé parameter $\lambda^{(1)}$ for the solid

Table 1
Values of physical parameters for the solid phase (cortical bone) as given in [17,7,39].

Parameter	Symbol	Value
Solid bulk modulus	$K^{(s)}$	2.04×10^{10} Pa
Solid shear modulus	$\mu^{(1)}$	0.833×10^{10} Pa
Solid Young's modulus	E	2.2×10^{10} Pa
Poisson's ratio	ν	0.32
Lamé coefficient	$\lambda^{(1)}$	1.48×10^{10} Pa
Frame material density	$\rho^{(s)}$	1960 kg m^{-3}
Solid frame viscosity	$\lambda^{(2)}$	197 Pa s
Solid frame viscosity	$\mu^{(2)}$	35 Pa s

Table 2
Values of physical parameters for the fluid phase (blood marrow) as given in [17,7,39].

Parameter	Symbol	Value
Fluid bulk modulus	$K^{(f)}$	2×10^{9} Pa
Pore fluid density	$\rho^{(f)}$	950 kg m^{-3}
Sound speed in fluid	c	1451 m s^{-1}
Pore fluid viscosity	η	1.46 N s m^{-2}

phase is defined by

$$\lambda^{(1)} = \frac{\nu E}{(1+\nu)(1-2\nu)}.$$

The viscosity coefficients $\lambda^{(2)}$, $\mu^{(2)}$ and η are derived in the following Appendix [54,55].

In this section, we first test the performance of the PML, and then examine ultrasound attenuation through bone samples obtained from CT-scanned images and simulated random realizations, as described above.

7.1. Perfectly matched layer

Let us consider a purely solid material ($\beta=0$). In the case of one-dimensional wave propagation without viscosity, Eqs. (3.7)–(3.9) with free-surface boundary conditions reduce to the wave equation:

$$\partial_t^2 u_x = \frac{\lambda^{(1)}+2\mu^{(1)}}{\rho^{(s)}}\partial_x^2 u_x, \tag{7.1}$$

for the displacement u_x, with reflecting boundary condition $\partial_x u_x = 0$ at both endpoints $x=0$ and $x=L_x$. The corresponding stress and velocity are determined by

$$\tau_{xx} = (\lambda^{(1)}+2\mu^{(1)})\partial_x u_x, \quad v_x = \partial_t u_x.$$

Given initial conditions

$$u_x = f(x), \quad \partial_t u_x = 0,$$

and considering only the first rebound off the endpoints, Eq. (7.1) admits the exact d'Alembert solution:

$$u_x = \tfrac{1}{2}[f(x+c^{(s)}t)+f(x-c^{(s)}t)],$$
$$v_x = \tfrac{1}{2}c^{(s)}[f'(x+c^{(s)}t)-f'(x-c^{(s)}t)],$$
$$\tau_{xx} = \tfrac{1}{2}(\lambda^{(1)}+2\mu^{(1)})[f'(x+c^{(s)}t)+f'(x-c^{(s)}t)],$$

if $x-c^{(s)}t>0$, $x+c^{(s)}t<L_x$, and

$$u_x = \tfrac{1}{2}[f(2L_x-x-c^{(s)}t)+f(c^{(s)}t-x)],$$
$$v_x = -\tfrac{1}{2}c^{(s)}[f'(2L_x-x-c^{(s)}t)-f'(c^{(s)}t-x)],$$
$$\tau_{xx} = -\tfrac{1}{2}(\lambda^{(1)}+2\mu^{(1)})[f'(2L_x-x-c^{(s)}t)+f'(c^{(s)}t-x)],$$

otherwise, where

$$c^{(s)} = \sqrt{\frac{\lambda^{(1)}+2\mu^{(1)}}{\rho^{(s)}}},$$

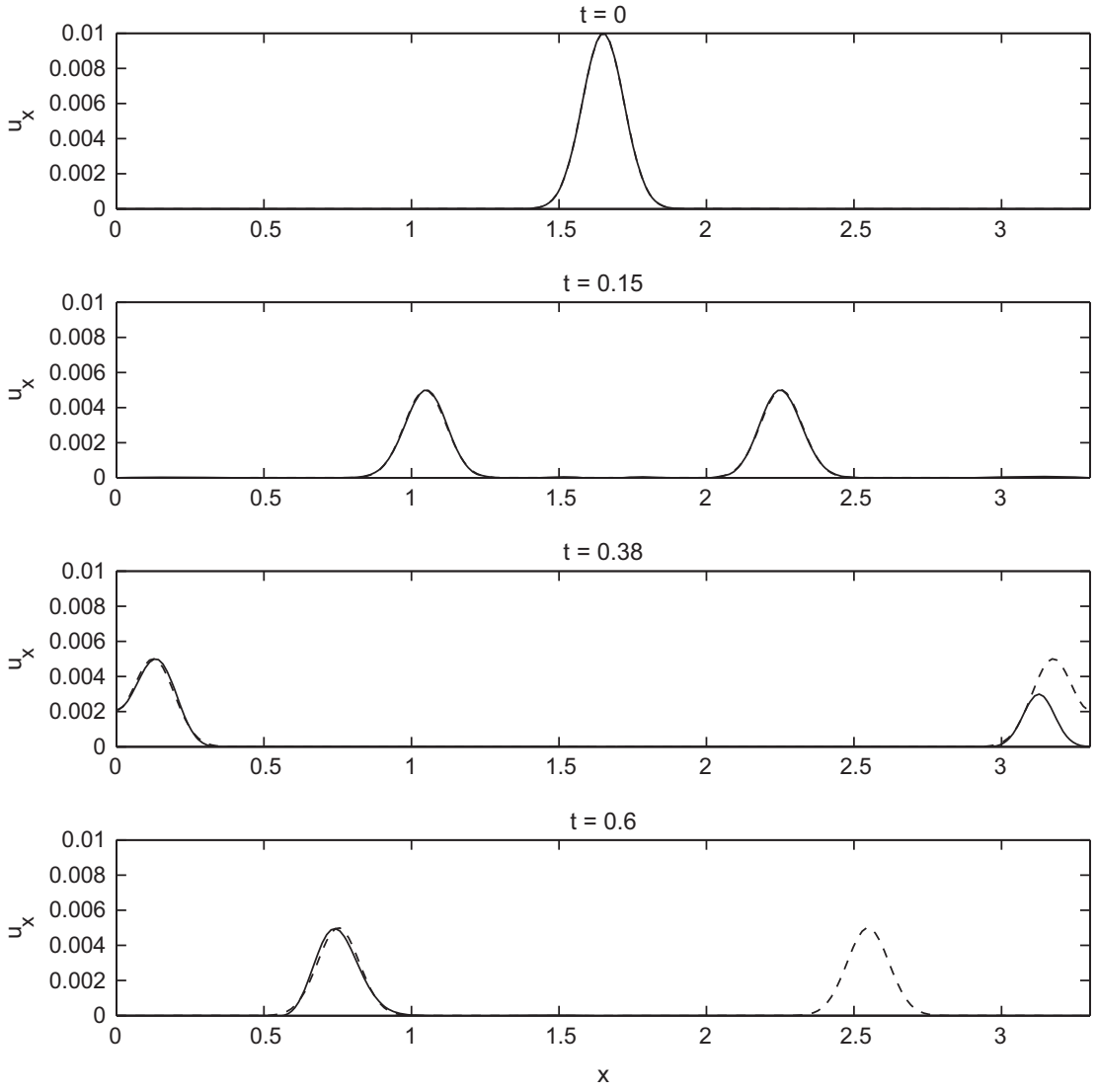

Fig. 2. Profile of displacement u_x in the cross-section $y=L_y/2$ at $t=0$, 0.15, 0.38, 0.6. The solid line corresponds to the numerical solution (with PML at $x=L_x$) while the dashed line corresponds to the exact solution (without PML).

and the primes denote differentiation with respect to the argument of the function f.

To compare with this exact solution, we perform numerical simulations of (4.1) and (4.2) using initial conditions

$$u_x(x,y,0) = f(x) = 0.01e^{-100(x-(L_x+\delta)/2)^2},$$

$$v_x(x,y,0) = 0,$$

and

$$\tau_{xx}(x,y,0) = (\lambda^{(1)}+2\mu^{(1)})f'(x) = -(\lambda^{(1)}+2\mu^{(1)})(2x-L_x-\delta)e^{-100(x-(L_x+\delta)/2)^2},$$

which are invariant in the y-direction. The computational domain is a square with sides $L_x = L_y = 3$. A PML of width $\delta = 20\Delta x$ with damping parameters $R = 10^{-4}$ and $V = c^{(s)}$ is placed next to the right side $x = L_x$.

Figs. 2–4 show the comparison between exact (without PML) and numerical (with PML) profiles of u_x, v_x and τ_{xx} in the cross-section $y = L_y/2$ at various values of t. The spatial resolution is $N_x \times N_y = 200 \times 200$, where N_x and N_y denote the number of grid points in the x- and y-directions respectively, and the time step is $\Delta t = 5 \times 10^{-4}$. This simulation includes the splitting of the initial condition into left- and right-moving components, as well as their propagation to and bouncing off the sides of the domain. For all three variables, the profile of their left component, its propagation speed and the reflecting boundary condition at $x=0$, are well reproduced numerically. In particular, neither visible spurious oscillations nor significant numerical diffusion are observed. Of course, a better agreement can be obtained by increasing the spatial resolution. By contrast, the right component is quickly absorbed as it travels through the PML and no reflection is discernible from the right side. We checked that the amplitude ratio of the right (damped) wave to the left (undamped) wave is about 10^{-4} at $t=0.6$, which agrees with the specified value of R and with results of Collino and Tsogka [49] for the PML width being considered. This test confirms that our implementation of the PML is effective at significantly reducing wave reflection from domain boundaries.

7.2. Ultrasound attenuation

It is well known that ultrasound propagation through cancellous bone experiences attenuation [56,57,39]. This attenuation is more pronounced at higher frequencies and also increases with bone volume fraction (i.e. bone density). In this section, we numerically check these features of ultrasound attenuation for bone samples obtained from both CT-scanned images and simulated random realizations. Hereinafter, for convenience, we refer to 'real bone' samples in our study as those reconstructed from CT-scanned images of real human calcaneus and to 'synthetic bone' samples as those obtained from random realizations simulated by the turning bands method.

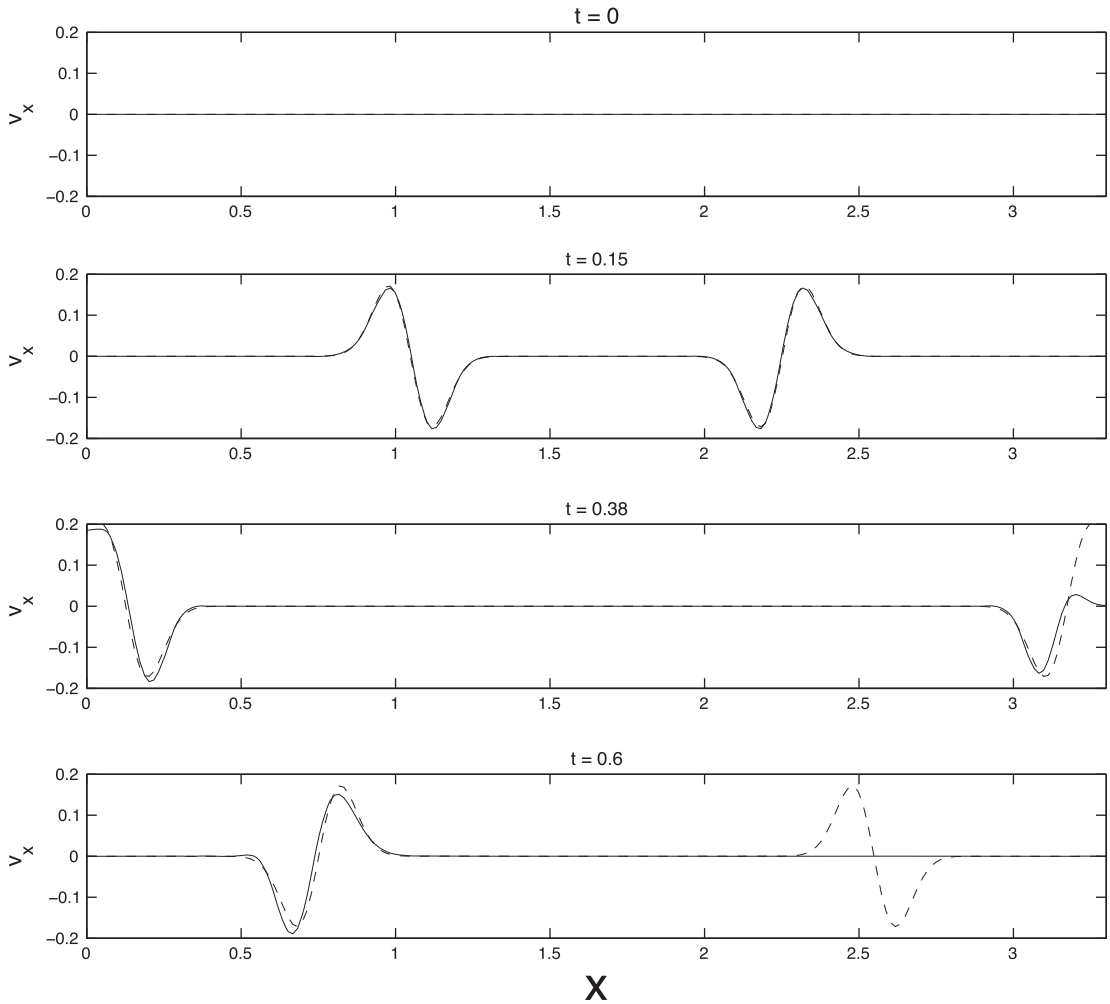

Fig. 3. Profile of velocity v_x in the cross-section $y = L_y/2$ at $t=0$, 0.15, 0.38, 0.6. The solid line corresponds to the numerical solution (with PML at $x = L_x$) while the dashed line corresponds to the exact solution (without PML).

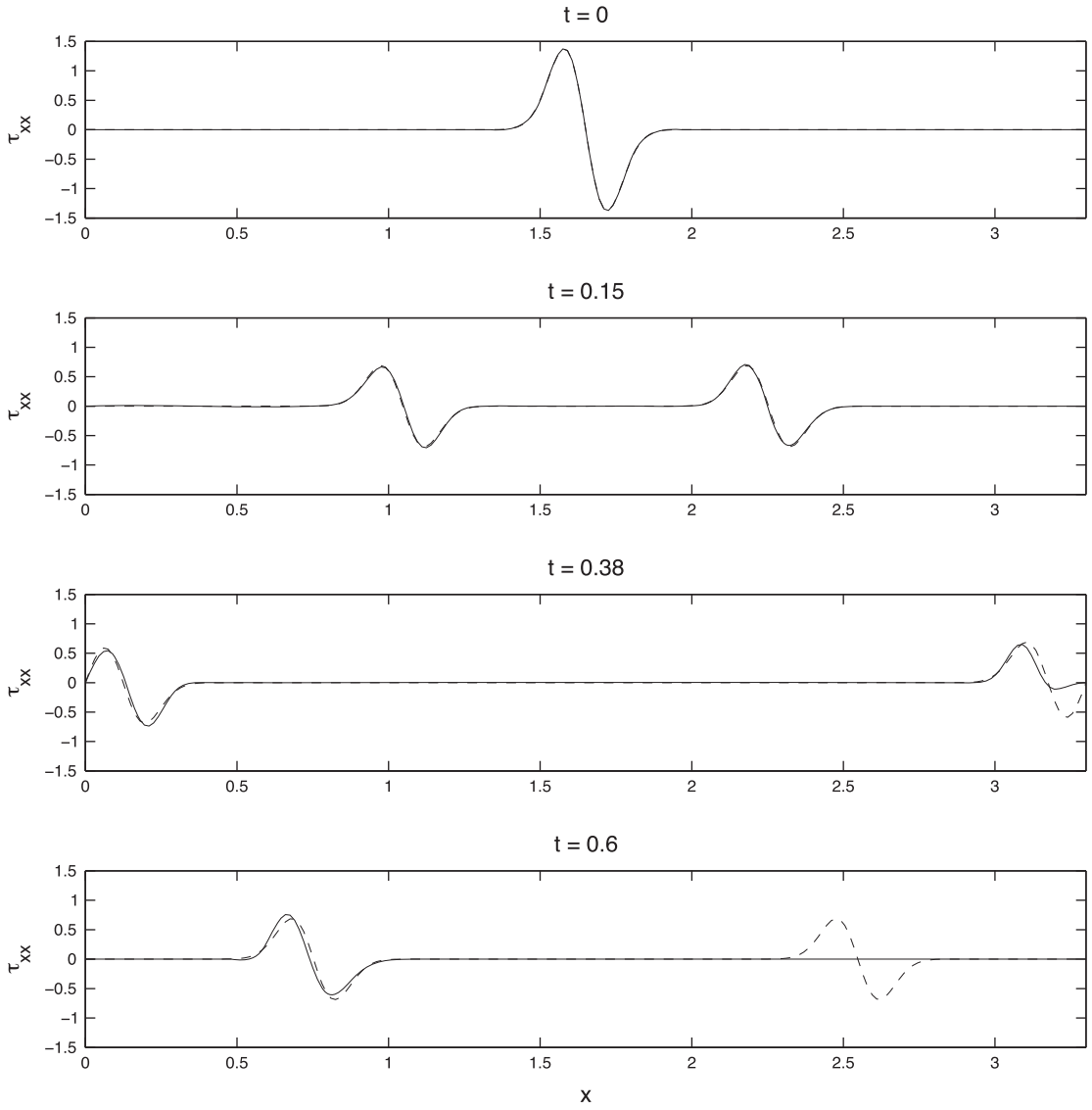

Fig. 4. Profile of stress τ_{xx} in the cross-section $y = L_y/2$ at $t = 0$, 0.15, 0.38, 0.6. The solid line corresponds to the numerical solution (with PML at $x = L_x$) while the dashed line corresponds to the exact solution (without PML).

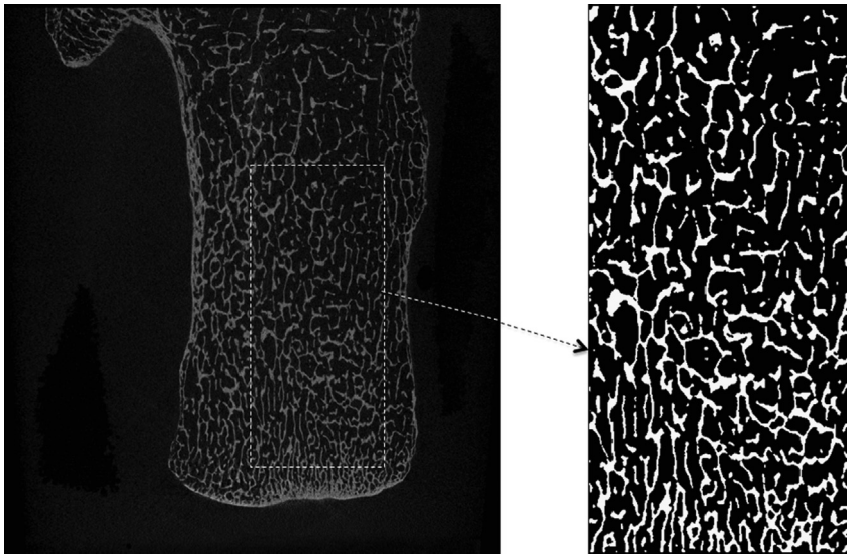

Fig. 5. Left: CT-scanned image of human calcaneus. Right: binary mapping of a rectangular 1 cm $\times$ 2 cm cross-section along the calcaneal bone. The white area is the trabecular matrix while the black area is the interstitial space.

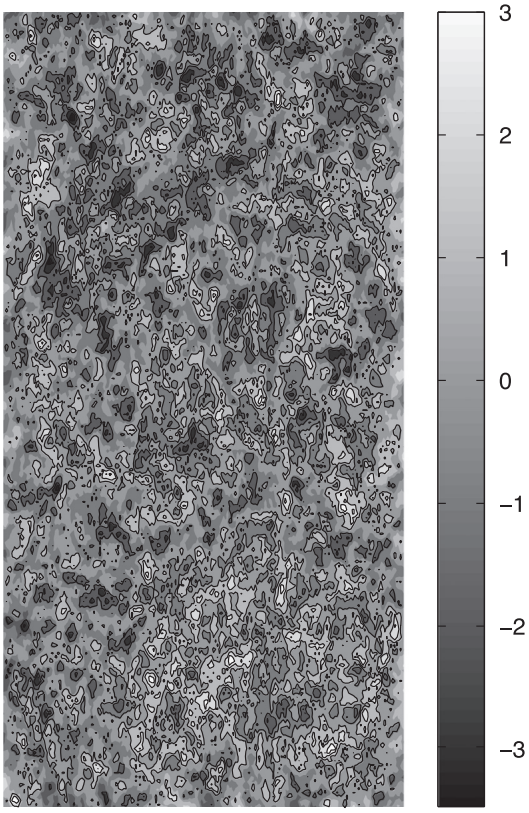

Fig. 6. Two-dimensional 1 cm × 2 cm random field simulated by the turning bands method for an exponential covariance function.

As mentioned earlier, we concentrate on two-dimensional rectangular bone samples which are 1 cm long in the x-direction and 2 cm wide in the y-direction. The incoming pulse is generated by a pressure source located on the left side of the domain ($x=0$) and defined by

$$\tau_{xx}(0,y,t) = P\ \sin(2\pi f_c t) e^{-(t-5t_0/2)^2/t_0^2},$$

where $t_0 = 1/f_c$ and f_c denotes the prescribed temporal frequency. The pressure is applied over the whole left side of the domain, and its amplitude is set to be $P=8$ kPa following [39,42]. A PML of width $\delta = 20\Delta x$ is attached to the right side. The spatial resolution $N_x \times N_y = 200 \times 200$ and time step $\Delta t = 10^{-4}$ are selected sufficiently fine so they can resolve well the excitation wavelength and period. The time step is also chosen based on the CFL condition for stability as derived in [43]. Since we expect the excitation to be primarily longitudinal, propagating from left to right in the x-direction, we focus our attention on u_x. The transverse displacement u_y (not shown here) is typically of an order of magnitude smaller than u_x. This direction of wave propagation is chosen to be perpendicular to the main orientation of the trabecular network in real bone (as indicated in Fig. 7(a)–(d)) so as to match the orientation of the ultrasound beam in *in vivo* clinical examinations.

Fig. 8 shows time series of a typical signal sent out by the source and received on the opposite side of the domain. For illustration, a snapshot of the corresponding two-dimensional profile at $t = 12$ μs is presented in Fig. 9. The irregular character of the medium is apparent from the two-dimensional profile of the signal. The one-dimensional profiles of u_x in Fig. 8 result from averaging over the transverse y-direction. We see that the waveform is overall preserved but its amplitude decreases as the wave travels through the domain. To quantify this effect, in particular its dependence on excitation frequency and bone volume fraction, we evaluate the attenuation coefficient α as defined by

$$\frac{A_2}{A_1} = e^{-\alpha L_x},$$

where A_1 (resp. A_2) is the input (resp. received) y-averaged amplitude of u_x and $L_x = 1$ cm.

Values of α for $\beta = 0.7, 0.75, 0.8, 0.85$ as functions of frequency f_c are reported in Figs. 10 and 11. Both real and synthetic bone samples are examined. A number of observations can be made from these figures. First, in all cases, α seems to increase linearly with f_c over the wide range 0.5–2 MHz, which is consistent with other experimental [57,22,30] and numerical [37] results. In particular, Wear [30] also observed linear dependence (without apparent breakpoint) from 0.4 MHz up to at least 1.7 MHz for human calcaneus *in vitro*. For all four values of β considered, attenuation is slightly stronger in real bones than in synthetic ones but their respective values of α are overall comparable. This suggests that randomly generated bone samples are a good approximation to real ones, at least as far as wave propagation in the x-direction is concerned here. Figs. 10 and 11 also compare cases with and without viscosity (by setting $\lambda^{(2)} = \mu^{(2)} = \eta = 0$). As expected, attenuation is found to be larger in viscous cases than in non-viscous ones, and is more pronounced at higher frequencies, but overall the difference in α between these two cases is almost negligible for both real and synthetic bones. Our two-dimensional results support the conclusion drawn by Bossy et al. [37], based on three-dimensional numerical simulations without viscosity, that ultrasound attenuation in cancellous bone is mainly attributable to scattering by the complex trabecular structure.

Assuming a linear dependence of attenuation on frequency, as suggested by our numerical results, we can calculate the nBUA parameter defined as the slope of a linear fit to the data:

$$\alpha = \alpha_0 + \mathrm{nBUA} \times f.$$

Here this linear fit is applied to the whole range $f_c \in [0.5, 2]$ MHz. Normalized nBUA values are known to be strongly and positively correlated with bone volume fraction (i.e. bone density) BV $= 1-\beta$ [46,58,59], which is well illustrated in Fig. 12. A total of 60 bone samples (30 real and 30 synthetic bone samples), including viscous effects, are used for this plot. The nBUA values for real bone are overall larger than those for synthetic bone but they remain comparable, with a difference of about 15%, and they follow a similar increasing trend. These results are again consistent with those reported in [30,37], however we note that the nBUA values found in [37] tend to grow faster with bone volume fraction than our values do. For example, their nBUA value is about 30 dB/cm/MHz for BV=20% while ours (for real bone) is about 13 dB/cm/MHz for the same volume fraction. This may be attributed to the complex three-dimensional trabecular architecture used in their numerical simulations, which promotes stronger ultrasound scattering than in two dimensions. The similarities between the nBUA graphs for real and synthetic bones in Fig. 12 (and with the nBUA graph in [37]) further support the fact that the present random model can generate realistic bone specimens for ultrasound interrogation.

Another physical parameter which correlates well with bone volume fraction is the SOS [58], as indicated in Fig. 13. For $f_c = 1$ MHz and a given porosity, by recording the peak times t_1 and t_2 of the emitted and received y-averaged pulses (on the left and right sides of the domain) respectively, as shown in Fig. 8, we can estimate the speed of sound through the bone sample as

$$\mathrm{SOS} = \frac{L_x}{t_2 - t_1}.$$

Observations similar to those for the nBUA parameter can be made here. In particular, for high porosities, our SOS values are found to

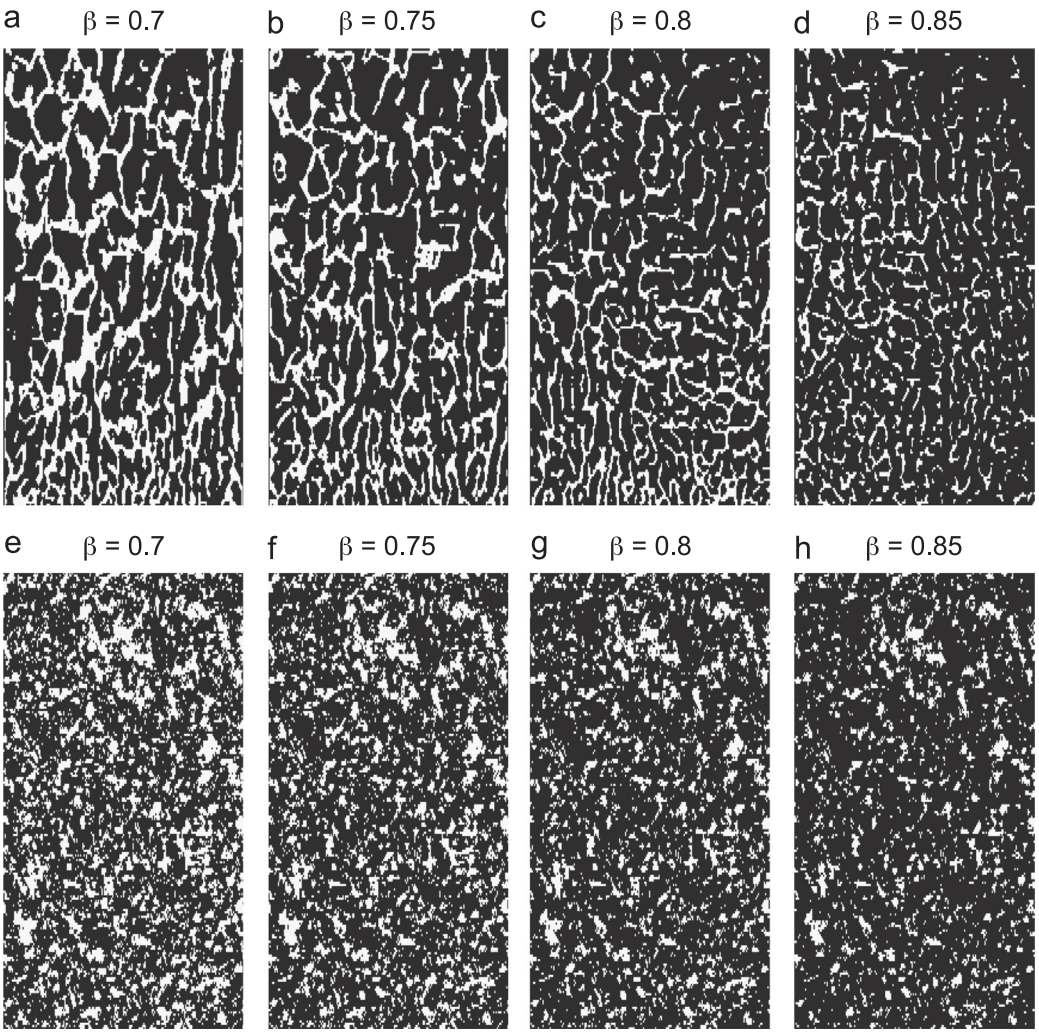

Fig. 7. Top: 'real' bone samples of porosity (a) β=0.7, (b) 0.75, (c) 0.8, (d) 0.85 reconstructed from CT-scanned images of human calcaneus. Bottom: 'synthetic' bone samples of porosity (e) β=0.7, (f) 0.75, (g) 0.8, (h) 0.85 obtained from random realizations simulated by the turning bands method. The size of each sample is 1 cm $\times$ 2 cm.

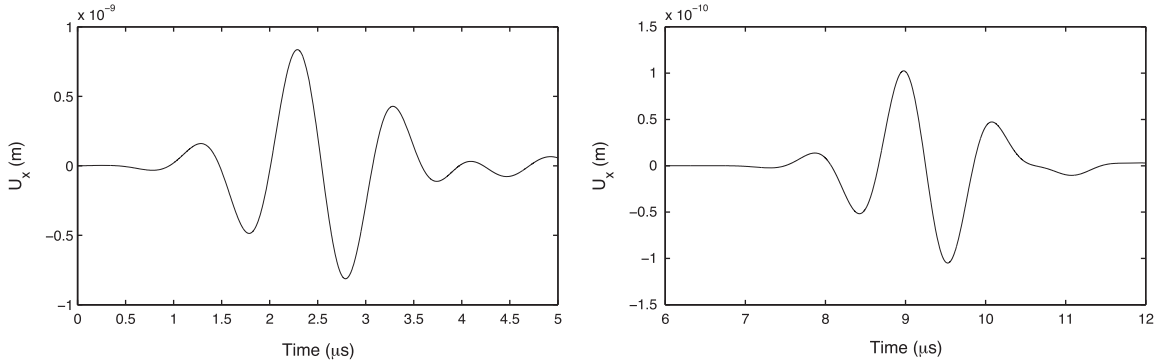

Fig. 8. Left: time series of a typical y-averaged signal sent out by the pressure source on the left side of the domain. The graph represents the profile of displacement u_x. Right: time series of the corresponding signal received on the right side of the domain.

increase over a range close to that reported by Bossy et al. [37] (i.e. $\sim$1500–1600 m/s). When comparing real and synthetic bones, their respective SOS values tend to deviate from each other as BV increases. However, this deviation remains small within 5% of a representative value, say 1500 m/s. As far as the nBUA and SOS are concerned, our two-dimensional results for real bone are overall closer to the three-dimensional results of Bossy et al. [37]. This may be explained by the fact that their numerical simulations used three-dimensional bone samples reconstructed from CT scans of real human femur. We note again that, unlike our acoustic model, the one of Bossy et al. [37] did not account for viscous dissipation in cancellous bone. Therefore, the similarity of results clearly points to scattering as a major cause for ultrasound attenuation in either two or three dimensions. This is consistent with results of Naili et al. [60] who proposed an *in vivo* model for cortical bone, and showed that viscous absorption in the surrounding fluid tissues is negligible while bone viscoelastic properties may have a significant effect on the acoustic response.

8. Conclusions

In this study, we perform numerical simulations on two-dimensional bone samples obtained from CT scans of human calcaneus and from realizations of a random process, to assess the phenomenon of ultrasound attenuation including its dependence on excitation frequency and bone volume fraction. We examine in particular the contribution of scattering by the trabecular microstructure. Another objective is to test the random algorithm, based on the turning bands method, in view of creating a large catalog of synthetic bone specimens to be used for the inverse problem of recovering effective bone parameters from acoustic interrogation.

Hoffmeister et al. [61] found that, in the range 0.5–1 MHz, the nBUA exhibits a significant correlation with the anterior–posterior and medial–lateral directions but not in the superior–inferior orientations. A breakpoint in the slopes was observed at about 1 MHz, whereas other researchers observed one at about 400 kHz. Other studies however reported measurable nonlinear attenuation at frequencies below 400 kHz for unfatted bone from human cadavers [28]. Our numerical results show a linearly increasing dependence of ultrasound attenuation on incoming frequency in both cases, over the wide range 0.5–2 MHz. We have not discerned any noticeable breakpoint in this range of frequencies, consistent with *in vitro* experiments of Wear [30]. Attenuation and propagation speed are also found to increase with bone volume fraction for both types of bone samples. Our two-dimensional simulations support the three-dimensional numerical results of Bossy et al. [37] that scattering by the complex trabecular network plays a major role in ultrasound attenuation. Moreover our random model is shown to be able to mimic realistic bone specimens for ultrasound interrogation, especially at high porosities and in the transverse direction of the trabecular network.

Our acoustic model for cancellous bone includes viscosity in both fluid and solid phases with physically relevant parameters. The role played by bone marrow in ultrasound measurement for bone is still under debate. Some researchers [62,63] claim that taking into account marrow viscosity leads only to minor differences on the effective attenuation and dispersion. Nicholson and Bouxsein [64] made quantitative ultrasound transmission and backscatter experiments on 46 human cancellous bone specimens (both water filled and *in vivo*). They concluded that the potential impact of bone marrow should be considered when interpreting quantitative ultrasound measurement. In simulated studies using a variant of the Biot model, we found that using a shear-thinning fluid, which we believe represents more accurately the blood-marrow interstitial fluid, yields results quite different from the case of water as the interstitial fluid [65]. See also the works [66–68] which support our claim.

We plan in the future to compare three-dimensional, transversely isotropic (i.e. orthotropic) random simulations in conjunction with three-dimensional CT scans of actual bone samples. Transverse isotropy can be included in the random realizations by

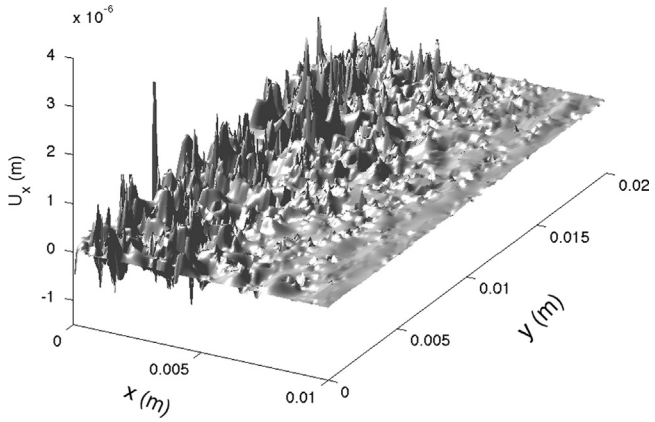

Fig. 9. Two-dimensional snapshot of displacement u_x, corresponding to Fig. 8, at $t = 12$ μs. For clarity, the values of u_x are magnified by a factor of 10^3.

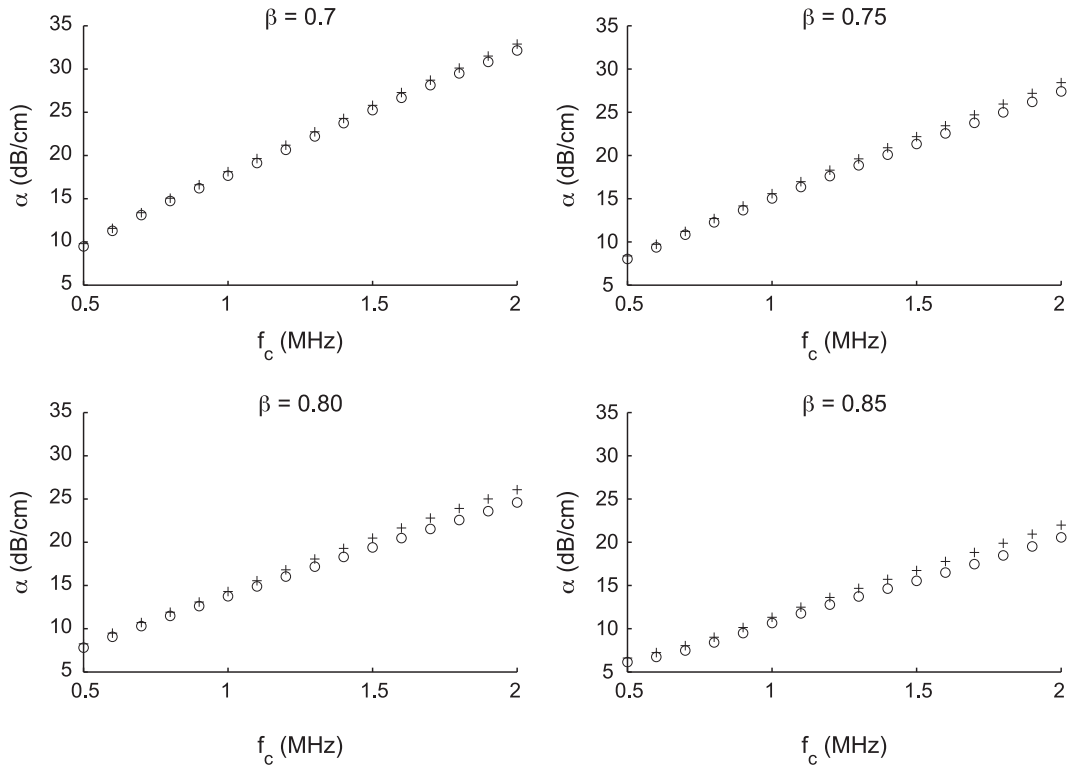

Fig. 10. Attenuation coefficient α versus frequency f_c for real bone samples of porosity β=0.7, 0.75, 0.8, 0.85 with (crosses) and without (circles) viscosity.

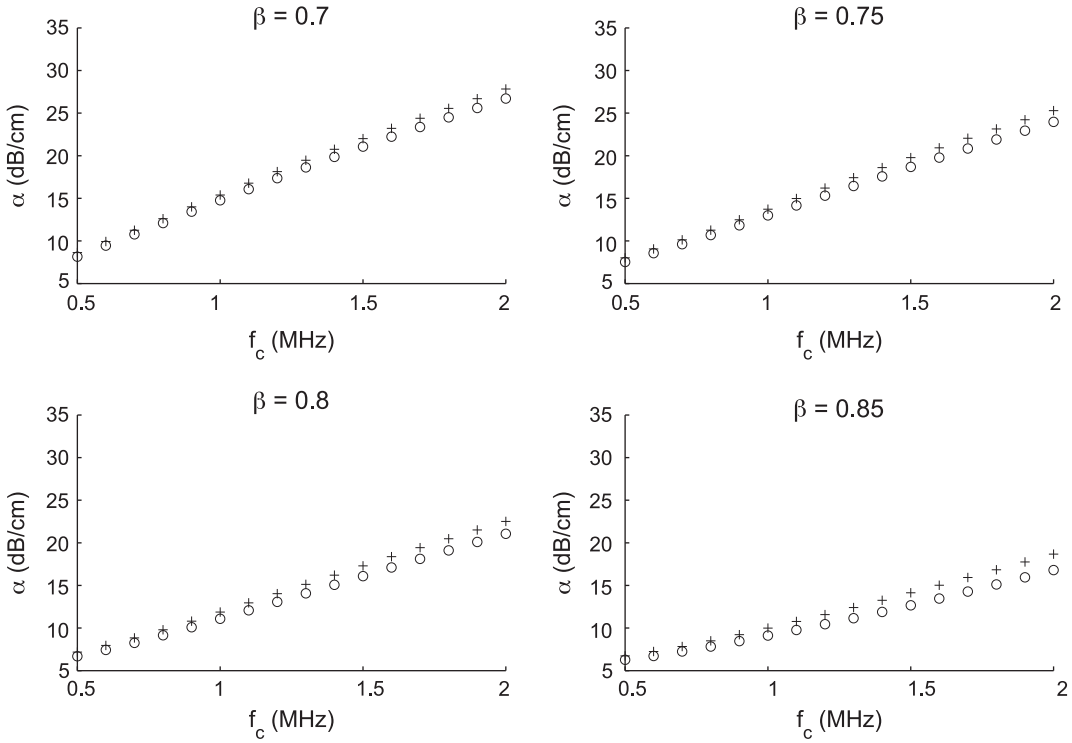

Fig. 11. Attenuation coefficient α versus frequency f_c for synthetic bone samples of porosity $\beta = 0.7, 0.75, 0.8, 0.85$ with (crosses) and without (circles) viscosity.

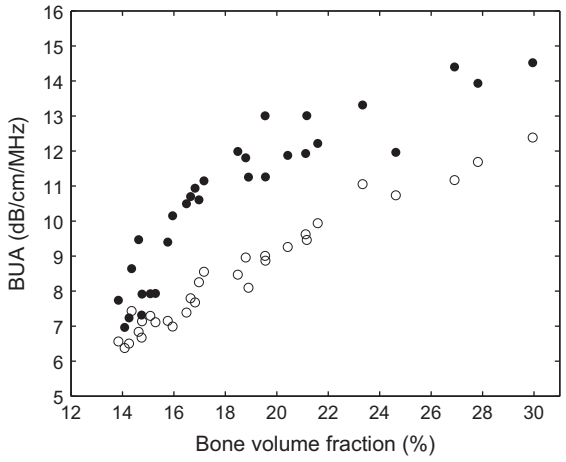

Fig. 12. Normalized BUA versus bone volume fraction for 30 real bone samples (solid dots) and 30 synthetic bone samples (circles).

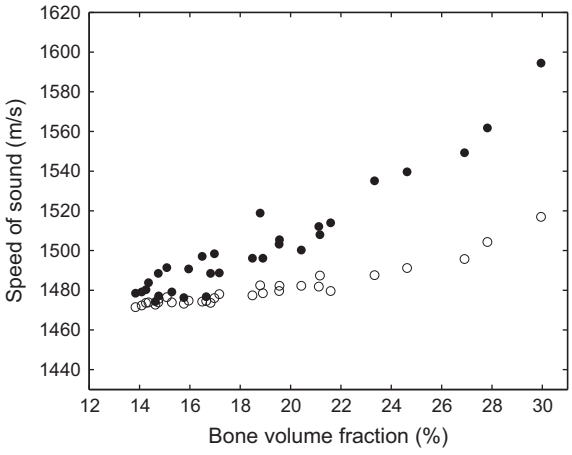

Fig. 13. Speed of sound at $f_c = 1$ MHz versus bone volume fraction for 30 real bone samples (solid dots) and 30 synthetic bone samples (circles).

allowing the covariance function (which is a prescribed quantity in the turning bands method) to exhibit angular dependence. In this case, we expect that the comparison may be even more satisfactory than for two-dimensional samples. Moreover, we intend to incorporate in our model non-Newtonian interstitial fluids as mentioned above. A long-term goal is to emulate three-dimensional simulations of the experiments described in [17,69] and, to accomplish this, we need to use the effective acoustic propagation equations. Using homogenization theory, we showed that the effective equations are equivalent, up to an order of magnitude of 10^{-3}, to a Biot system [51–53]. Having effective equations allows us to pose a viable inverse problem for three-dimensional samples by measuring acoustic pressure data at different locations in the water tank [70]. Such problems are solved by minimizing the difference with respect to an appropriate norm between the measured acoustic pressure and the acoustic pressure predicted by the effective equations over a set of effective parameters (such as bone porosity and other elasticity coefficients) related to material parameters as given in Tables 1 and 2. These effective parameters can be evaluated from bone samples as shown in [43], and having a large catalog of samples is crucial for accurately solving the inverse problem. This has important clinical implications for better assessment of bone quality and for better diagnosis of osteoporosis using quantitative ultrasound techniques.

To our knowledge, no three-dimensional inversions have to date been made despite the scientific importance of work done in [10–12,26,37,70,46,71,72]. These considered either one-dimensional inversion approaches or three-dimensional direct problems, i.e. by observing wave propagation through the matrix of one of the CT scans. The inverse problem that we have in mind should not be confused with the reconstruction of microstructure from CT scans obtained using a synchrotron or with the correlation analysis performed on macroscopic parameters [37,46]. Our two-dimensional inversion

approach [7,8] is still state of the art for inverse problems for cancellous bone. It is our intent to extend this method to fully three-dimensional bone samples.

Conflict of interest statement

The authors have no conflict of interests to declare.

Acknowledgments

This research was partially supported by the NSF through Grant no. DMS-0920850 and the Simons Foundation through Grant no. 246170. We thank Dr. Luis Cardoso from The City University of New York for kindly providing us with the CT-scanned images of bone used in the present study.

Appendix A. Calculation of viscosity coefficients

In this Appendix, we derive physically relevant values for the viscosity coefficients used in our numerical simulations of ultrasound propagation through cancellous bone. For the solid phase, let α_L and α_T be the attenuation rates associated with the longitudinal and transverse modes, respectively. A relation between attenuation rate and viscosity coefficient for the longitudinal mode is given by

$$\alpha_L = \frac{\eta_{11}\omega^2}{2c_L(\lambda^{(1)}+2\mu^{(1)})}, \tag{A.1}$$

provided $\omega \gg \alpha_L c_L$, where $c_L = \sqrt{(\lambda^{(1)}+2\mu^{(1)})/\rho^{(s)}}$ is the speed of sound in the longitudinal direction. A similar relation for the transverse mode can be written as

$$\alpha_T = \frac{\eta_{66}\omega^2}{2c_T\mu^{(1)}}, \tag{A.2}$$

provided $\omega \gg \alpha_T c_T$, where $c_T = \sqrt{\mu^{(1)}/\rho^{(s)}}$ is the speed of sound in the transverse direction. Using parameter values listed in Table 1 together with values of α_L and α_T reported in [73,74], we find $\alpha_L c_L = 1.68 \times 10^5\ \mathrm{s}^{-1}$ and $\alpha_T c_T = 8.25 \times 10^4\ \mathrm{s}^{-1}$ while $\omega = 2\pi \times 10^6\ \mathrm{s}^{-1}$ for a characteristic ultrasonic frequency $f_c = 1$ MHz, so the conditions for (A.1) and (A.2) are met here. From (A.1) and (A.2) and the fact that

$$\eta_{12} = \eta_{11} - 2\eta_{66}, \tag{A.3}$$

in the isotropic case, we can evaluate the viscosity coefficients η_{12}, η_{11}, η_{66} (see Table A1) and, accordingly,

$$\lambda^{(2)} = \eta_{12}, \quad \mu^{(2)} = \eta_{66}.$$

Similarly, for the fluid phase, a relation between attenuation coefficient and viscosity coefficient reads as follows:

$$\alpha_f = \frac{\eta\omega^2}{2cK^{(f)}}, \tag{A.4}$$

provided $\omega \gg \alpha_f c$, where $c = \sqrt{K^{(f)}/\rho^{(f)}}$ with $K^{(f)}$ being the fluid bulk modulus. Using parameter values from Table 2 and α_f from [75], we can check that $\alpha_f c = 1.45 \times 10^4\ \mathrm{s}^{-1} \ll \omega$ for a frequency $f_c = 1$ MHz. Recall that $\lambda^{(3)} = c^2\rho^{(f)}$, $\lambda^{(4)} = 0$, $\mu^{(3)} = 0$ and $\mu^{(4)} = \eta$ for the fluid phase. Table A2 lists the value of η obtained from (A.4), which is close to the value $\eta = 1.5$ Pa s used in [17].

Table A1
Attenuation coefficients at $f_c = 1$ MHz and corresponding viscosity coefficients for the solid phase: α_L is taken from [73], α_T is taken from [74], η_{11} and η_{66} are evaluated from (A.1) and (A.2) while η_{12} is calculated from (A.3).

α_L (dB cm^{-1})	α_T (dB cm^{-1})	η_{11} (Pa s)	η_{12} (Pa s)	η_{66} (Pa s)
4.2	4	267	197	35

Table A2
Attenuation coefficient at $f_c = 1$ MHz and corresponding viscosity coefficient for the fluid phase: α_f is taken from [75] and η is evaluated from (A.4).

α_f (dB cm^{-1})	c (m s^{-1})	η (Pa s)
1	1451	1.46

References

[1] R. Ashman, J. Cowin, C. Turner, Elastic properties of cancellous bone: measurement by an ultrasonic technique, J. Biomech. 20 (1987) 979–986.
[2] R. Ashman, J. Rho, Elastic modulus of trabecular bone material, J. Biomech. 21 (1988) 177–181.
[3] E. Bossy, M. Talmant, P. Laugier, 2d simulation of the axial transmission technique on a cortical bone plate, Acoust. Imaging 26 (2002) 69–76.
[4] E. Bossy, M. Talmant, P. Laugier, Effect of bone cortical thickness on velocity measurements using ultrasonic axial transmission: a 2D simulation study, J. Acoust. Soc. Am. 112 (2002) 297–307.
[5] J. Buchanan, R. Gilbert, Measuring osteoporosis using ultrasound, Adv. Scatt. Biomech. Eng. (2004) 484–494.
[6] J. Buchanan, R. Gilbert, K. Khashanah, Determination of the parameters of cancellous bone using low frequency acoustic measurements, J. Comput. Acoust. 12 (2004) 99–126.
[7] J. Buchanan, R. Gilbert, Determination of the parameters of cancellous bone using high frequency acoustic measurements, Math. Comput. Model. 45 (2007) 281–308.
[8] J. Buchanan, R. Gilbert, Determination of the parameters of cancellous bone using high frequency acoustic measurements ii: inverse problems, J. Comput. Acoust. 15 (2007) 199–220.
[9] S. Chaffai, G. Berger, P. Laugier, Frequency variation of ultrasonic attenuation coefficient of cancellous bone between 0.2 and 2.0 MHz, in: Proceedings of 1998 IEEE, Ultrasonics Symposium, vol. 2, IEEE, 1998, pp. 1397–1400.
[10] S. Chaffai, V. Roberjot, F. Peyrin, G. Berger, P. Laugier, Frequency dependence of ultrasonic backscattering in cancellous bone: autocorrelation model and experimental results, J. Acoust. Soc. Am. 108 (2000) 2403–2411.
[11] P. Droin, P. Laugier, G. Berger, Ultrasonic attenuation and dispersion of cancellous bone in the frequency range 200–600 kHz, Acoust. Imaging 23 (1997) 157–162.
[12] P. Droin, G. Berger, P. Laugier, Velocity dispersion of acoustic waves in cancellous bone, IEEE Trans. Ultrason. Ferroelectr. Freq. Control 45 (1998) 581–592.
[13] Z. Fellah, J. Chapelon, S. Berger, W. Lauriks, C. Depollier, Ultrasonic wave propagation in human cancellous bone: application of Biot theory, J. Acoust. Soc. Am. 116 (2004) 61–73.
[14] M. Fellah, Z. Fellah, F. Mitri, E. Ogam, C. Depollier, Transient ultrasound propagation in porous media using Biot theory and fractional calculus: application to human cancellous bone, J. Acoust. Soc. Am. 133 (2013) 1867–1881.
[15] T. Haire, C. Langton, Biot theory: a review of its application to ultrasound propagation through cancellous bone, Bone 24 (1999) 291–295.
[16] M. Hobatho, J. Rho, R. Ashman, Atlas of mechanical properties of human cortical and cancellous bone, J. Biomech. 25 (1992) 669.
[17] A. Hosokawa, T. Otani, Ultrasonic wave propagation in bovine cancellous bone, J. Acoust. Soc. Am. 101 (1997) 1219.
[18] M. Kaczmarek, M. Pakuła, J. Kubik, Multiphase nature and structure of biomaterials studied by ultrasounds, Ultrasonics 38 (2000) 703–707.
[19] T. Kundu, Ultrasonic Nondestructive Evaluation: Engineering and Biological Material Characterization, CRC Press, Boca Raton, USA, 2004.
[20] R. Lakes, H. Yoon, J. Katz, et al., Slow compressional wave propagation in wet human and bovine cortical bone, Science 220 (1983) 513–515.
[21] C. Langton, C. Njeh, The Physical Measurement of Bone, Series in Medical Physics and Biomedical Engineering, Taylor & Francis, Bristol, UK, 2003.
[22] C. Langton, S. Palmer, R. Porter, The measurement of broadband ultrasonic attenuation in cancellous bone, Eng. Med. 13 (1984) 89–91.
[23] M. McKelvie, S. Palmer, The interaction of ultrasound with cancellous bone, Phys. Med. Biol. 36 (2000) 1331–1340.
[24] C. Njeh, Quantitative Ultrasound: Assessment of Osteoporosis and Bone Status, Martin Dunitz, London, UK, 1999.
[25] R. Othman, G. Gary, Dispersion identification using the fourier analysis of resonances in elastic and viscoelastic rods, in: Acoustics, Mechanics, and the Related Topics of Mathematical Analysis: CAES Du CNRS, Frejus, France, 18–22 June 2002, 2002, p. 229.
[26] F. Padilla, F. Peyrin, P. Laugier, Prediction of backscatter coefficient in trabecular bones using a numerical model of three-dimensional microstructure, J. Acoust. Soc. Am. 113 (2003) 1122–1129.

[27] J. Rho, An ultrasonic method for measuring the elastic properties of human tibial cortical and cancellous bone, Ultrasonics 34 (1996) 777–783.
[28] R. Strelitzki, J. Evans, On the measurement of the velocity of ultrasound in the os calcis using short pulses, Eur. J. Ultrasound 4 (1996) 205–213.
[29] K. Wear, Frequency dependence of ultrasonic backscatter from human trabecular bone: theory and experiment, J. Acoust. Soc. Am. 106 (1999) 3659–3664.
[30] K. Wear, Ultrasonic attenuation in human calcaneus from 0.2 to 1.7 MHz, IEEE Trans. Ultrason. Ferroelectr. Freq. Control 48 (2001) 602–608.
[31] K. Wear, Fundamental precision limitations for measurements of frequency dependence of backscatter: applications in tissue-mimicking phantoms and trabecular bone, J. Acoust. Soc. Am. 110 (2001) 3275–3282.
[32] J.L. Williams, Ultrasonic wave propagation in cancellous and cortical bone: prediction of some experimental results by Biot's theory, J. Acoust. Soc. Am. 91 (1992) 1106–1112.
[33] C. Langton, C. Njeh, R. Hodgskinson, J. Currey, Prediction of mechanical properties of the human calcaneus by broadband ultrasonic attenuation, Bone 18 (1996) 495–503.
[34] A. Hosokawa, Development of a numerical cancellous bone model for finite-difference time-domain simulations of ultrasound propagation, IEEE Trans. Ultrasonics Ferroelectr. and Frequ. Control 55 (2008) 558–562.
[35] J.L. Buchanan, R.P. Gilbert, M. Jung Ou, Wavelet decomposition of transmitted ultrasound wave through a 1-d muscle-bone system, J. Biomech. 44 (2011) 352–358.
[36] J. Buchanan, R. Gilbert, M. Ou, Recovery of the parameters of cancellous bone by inversion of effective velocities, and transmission and reflection coefficients, Inverse Probl. 27 (2011) 125006.
[37] E. Bossy, F. Padilla, F. Peyrin, P. Laugier, Three-dimensional simulation of ultrasound propagation through trabecular bone structures measured by synchrotron microtomography, Phys. Med. Biol. 50 (2005) 5545–5556.
[38] R. Graves, Simulating seismic wave propagation in 3D elastic media using staggered-grid finite differences, Bull. Seismol. Soc. Am. 86 (1996) 1091–1106.
[39] S. Ilic, K. Hackl, R. Gilbert, Application of the multiscale FEM to the modeling of cancellous bone, Biomech. Model. Mechanobiol. 9 (2010) 87–102.
[40] S. Ilic, K. Hackl, R. Gilbert, Application of a biphasic representative volume element to the simulation of wave propagation through cancellous bone, J. Comput. Acoust. 19 (2011) 111–138.
[41] S. Klinge, K. Hackl, R. Gilbert, Investigation of the influence of reflection on the attenuation of cancellous bone, Biomech. Model. Mechanobiol. 12 (2013) 185–199.
[42] R. Gilbert, P. Guyenne, J. Li, Simulation of a mixture model for ultrasound propagation through cancellous bone using staggered-grid finite differences, J. Comput. Acoust. 21 (2013) 1–28.
[43] R. Gilbert, P. Guyenne, J. Li, A viscoelastic model for random ultrasound propagation in cancellous bone, Comput. Math. Appl. 66 (2013) 943–964.
[44] G. Luo, J. Kaufman, A. Chiabrera, B. Bianco, J. Kinney, D. Haupt, J. Ryaby, R. Siffert, Computational methods for ultrasonic bone assessment, Ultrasound Med. Biol. 25 (1999) 823–830.
[45] A. Mantoglou, J. Wilson, The turning bands method for simulation of random fields using line generation by a spectral method, Water Resour. Res. 18 (1982) 1379–1394.
[46] S. Chaffai, F. Peyrin, S. Nuzzo, R. Porcher, R. Berger, P. Laugier, Ultrasonic characterization of human cancellous bone using transmision and backscatter measurements: relationships to density and microstructure, Bone 30 (2002) 229–237.
[47] F. Meziere, M. Muller, B. Dobigny, E. Bossy, A. Derode, Simulations of ultrasound propagation in random arrangements of elliptic scatterers: occurrence of two longitudinal waves, J. Acoust. Soc. Am. 133 (2013) 643–652.
[48] J.-P. Berenger, A perfectly matched layer for the absorption of electromagnetic waves, J. Comput. Phys. 114 (1994) 185–200.
[49] F. Collino, C. Tsogka, Application of the perfectly matched absorbing layer model to the linear elastodynamic problem in anisotropic heterogeneous media, Geophysics 66 (2001) 294–307.
[50] A. Tompson, R. Ababou, L. Gelhar, Implementation of the three-dimensional turning bands random field generator, Water Resour. Res. 25 (1989) 2227–2243.
[51] M. Fang, R. Gilbert, P. Guyenne, A. Vasilic, Numerical homogenization of the time-harmonic acoustics of bone: the monophasic case, Int. J. Multiscale Comput. Eng. 5 (2007) 461–471.
[52] M. Fang, R.P. Gilbert, A. Panchenko, A. Vasilic, Homogenizing the time-harmonic acoustics of bone: the monophasic case, Math. Comput. Model. 46 (2007) 331–340.
[53] R.P. Gilbert, A. Panchenko, A. Vasilic, Acoustic propagation in a random medium: the monophasic case, Math. Methods Appl. Sci. 33 (2010) 2206–2214.
[54] B. Auld, Acoustic Fields and Waves in Solids, vol. 1, Wiley, New York, USA, 1973.
[55] D. Royer, E. Dieulesaint, D. Morgan, Elastic Waves in Solids I: Free and Guided Propagation, Advanced Texts in Physics, Springer, Berlin, Germany, 2000.
[56] R. Lakes, H. Yoon, J. Katz, Ultrasonic wave propagation and attenuation in wet bone, J. Biomed. Eng. 8 (1986) 143–148.
[57] S. Chaffai, F. Padilla, G. Berger, P. Laugier, In vitro measurement of the frequency-dependent attenuation in cancellous bone between 0.2 and 2 MHz, J. Acoust. Soc. Am. 108 (2000) 1281–1289.
[58] D. Hans, M. Arlot, A. Schott, J. Roux, P. Kotzki, P. Meunier, Do ultrasound measurements on the os calcis reflect more the bone microarchitecture than the bone mass?: a two-dimensional histomorphometric study, Bone 16 (1995) 295–300.
[59] P. Nicholson, R. Muller, X. Cheng, P. Ruegsegger, G. Van der Perre, J. Dequeker, S. Boonen, Quantitative ultrasound and trabecular architecture in the human calcaneus, J. Bone Miner. Res. 16 (2001) 1886–1892.
[60] S. Naili, M.-B. Vu, Q. Grimal, M. Talmant, C. Desceliers, C. Soize, G. Haiat, Influence of viscoelastic and viscous absorption on ultrasonic wave propagation in cortical bone: application to axial transmission, J. Acoust. Soc. Am. 127 (2010) 2622–2634.
[61] B. Hoffmeister, S. Whitten, J. Rho, Low-megahertz ultrasonic properties of bovine cancellous bone, Bone 26 (2000) 635–642.
[62] C.F. Njeh, C. Langton, The effect of cortical endplates on ultrasound velocity through the calcaneus: an in vitro study, Br. J. Radiol. 70 (1997) 504–510.
[63] C.M. Langton, C.F. Njeh, R. Hodgskinson, J.D. Curey, Prediction of mechanical properties of human cancellous by broadbeam ultrasonic attenuation, Bone (1996) 495–503.
[64] P. Nicholson, M. Bouxsein, Bone marrow influences quantitative ultrasound measurements in human cancellous bone, Ultrasound Med. Biol. 28 (2002) 369–375.
[65] R.P. Gilbert, P. Guyenne, M. Yvonne Ou, A quantitative ultrasound model of the bone with blood as the interstitial fluid, Math. Comput. Model. 55 (2012) 2029–2039.
[66] C. Picart, J. Piau, H. Galliard, P. Carpentier, Human blood shear yield stress and its hematocrit dependence, J. Rheol. 42 (1998) 1–12.
[67] D. Sankar, K. Hemalatha, A non-newtonian fluid flow model for blood flow through a catheterized artery–steady flow, Appl. Math. Model. 31 (2007) 1847–1864.
[68] G. Thurston, Viscoelasticity of human blood, Biophys. J. 12 (1972) 1205–1217.
[69] K. Williams, D. Jackson, E. Thorsos, D. Tang, S. Schock, Comparison of sound speed and attenuation measured in a sandy sediment to predictions based on the Biot theory of porous media, IEEE J. Oceanic Eng. 27 (2002) 413–428.
[70] A. Saied, K. Raum, L. Leguerney, P. Laugier, Spatial distribution of anisotropic acoustic impedance as assessed by time-resolved 50-MHz scanning acoustic microscopy and its relation porosity in human cortical bone, Bone 43 (2008) 187–194.
[71] F. Padila, F. Jenson, V. Bousson, F. Peyrin, P. Laugier, Relationships of trabecular bone structure with quantitative ultrasound parameters: in vitro study on human proximal femur using transmission and backscatter measurements, Bone 42 (2008) 1193–1202.
[72] M. Sasso, G. Haiat, M. Talmant, P. Laugier, S. Naili, Singular value decomposition-based wave extraction in axial transmission: application to cortical bone ultrasonic characterization, IEEE Trans. Ultrasonics Ferroelectr. Freq. Control 55 (2008) 1328–1332.
[73] M. Sasso, G. Haiat, Y. Yamato, S. Naili, M. Matsukawa, Frequency dependence of ultrasonic attenuation in bovine cortical bone: an in vitro study, Ultrasound Med. Biol. 33 (2007) 1933–1942.
[74] B. Garcia, R. Cobbold, F. Foster, K. McNeill, Ultrasonic attenuation in bone, in: Ultrasonics Symposium, IEEE, 1978, pp. 327–330.
[75] S. Goss, R. Johnston, F. Dunn, Comprehensive compilation of empirical ultrasonic properties of mammalian tissues, J. Acoust. Soc. Am. 64 (1978) 423–457.